Imaging Interiors: An Implicit Solution to Electromagnetic Inverse Scattering Problems

Ziyuan Luo[1], Boxin Shi[2,3], Haoliang Li[4], and Renjie Wan[1]*

[1] Department of Computer Science, Hong Kong Baptist University
[2] State Key Laboratory for Multimedia Information Processing,
School of Computer Science, Peking University
[3] National Engineering Research Center of Visual Technology,
School of Computer Science, Peking University
[4] Department of Electrical Engineering, City University of Hong Kong
`ziyuanluo@life.hkbu.edu.hk`, `shiboxin@pku.edu.cn`, `haoliang.li@cityu.edu.hk`,
`renjiewan@hkbu.edu.hk`

Abstract. Electromagnetic Inverse Scattering Problems (EISP) have gained wide applications in computational imaging. By solving EISP, the internal relative permittivity of the scatterer can be non-invasively determined based on the scattered electromagnetic fields. Despite previous efforts to address EISP, achieving better solutions to this problem has remained elusive, due to the challenges posed by inversion and discretization. This paper tackles those challenges in EISP via an implicit approach. By representing the scatterer's relative permittivity as a continuous implicit representation, our method is able to address the low-resolution problems arising from discretization. Further, optimizing this implicit representation within a forward framework allows us to conveniently circumvent the challenges posed by inverse estimation. Our approach outperforms existing methods on standard benchmark datasets. Project page: https://luo-ziyuan.github.io/Imaging-Interiors.

Keywords: Electromagnetic inverse scattering problems · Implicit neural representations · Computational photography

1 Introduction

As electromagnetic waves can penetrate objects' surfaces, they play a key role in non-invasive imaging. Compared with modalities like X-ray and MRI, electromagnetic waves provide a potentially low-cost and safe approach [5, 24, 45] for non-invasive imaging.

Non-invasive imaging via electromagnetic waves needs to be completed by solving the Electromagnetic Inverse Scattering Problems (EISP). The typical scenario and the associated physical quantities of EISP are displayed in Fig. 1. In EISP, we need to infer the distribution of the scatterer's relative permittivity

---

* Corresponding author.
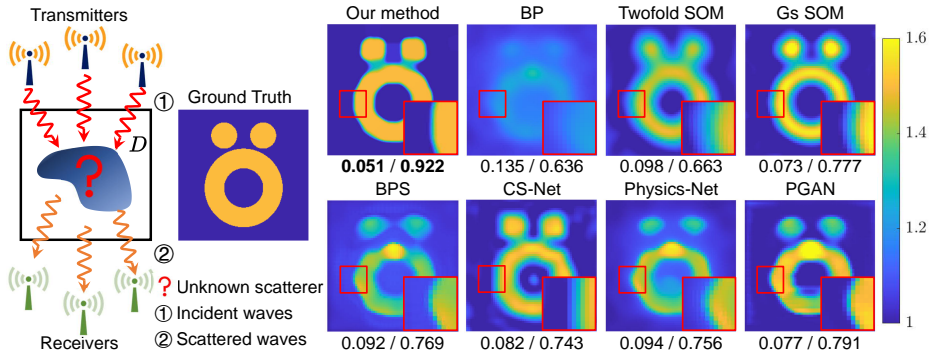
Fig. 1: The results of a standard test case [1,57] in EISP. In an EISP system, the scatterer in the enclosed space D is first illuminated by incoming electromagnetic waves emitted by transmitters and generates scattered fields. Then, the scattered fields measured by receivers are used to determine the scatterer's relative permittivity. We show results obtained by our method, BP [2], Twofold SOM [66], Gs SOM [8], BPS [57], CS-Net [50], Physics-Net [36], and PGAN [53]. The pixel values in the images indicate the values of the relative permittivity. RRMSE/SSIM values are shown below each figure.

from the measured scattered fields [43]. Then, the values of relative permittivity can be visualized to image the objects' internal structures.

However, solving EISP has never been an easy task. The first challenge comes from the **inverse** estimation process, where the scatterer's relative permittivity is derived from the measured scattered fields. The multiple scattering effects inherent to the EISP further significantly complicate this inverse estimation [9,34,68]. Furthermore, continuous spaces are usually discretized into finite elements or grids to facilitate numerical computations for electromagnetic computations. This process of **discretization** inherently leads to a loss of details and a decrease in image resolution for EISP [18,44]. This consequently poses challenges in accurately distinguishing internal small objects in close proximity.

The scattering mechanism is crucial in solving EISP [8,36]. Recent deep-learning-based methods [34,57] first obtain a rough image using traditional algorithms (*e.g.*, BP [2] shown in Fig. 1) and then refine this rough result using image-to-image translation networks. However, with the imaging process being divided into two distinct stages, the measured physical data are overlooked in the second phase, inevitably resulting in images of inferior quality (*e.g.*, BPS [57] and PGAN [53] shown in Fig. 1). Besides, as the relative permittivity distributions can vary greatly across different objects, a single network may be insufficient to reflect these differences. Therefore, a more appropriate approach is to optimize for each object while thoroughly considering the scattering mechanisms. Traditional methods like Twofold SOM [66] and Gs SOM [8] achieve this goal by discretizing continuous relative permittivity values into discrete variables expressed as to-be-optimized matrices [8,15,66]. However, they cannot address the low-resolution issues that arise from discretization, as shown in Fig. 1. Moreover,

these methods have difficulties in handling sparse measurement data, which usually leads to low reconstruction quality. Thus, we need a more powerful representation scheme beyond the discrete matrix form.

Since the scatterer's relative permittivity distribution used for imaging is intimately related to the spatial position [15], the envisioned approach should indicate such location-dependent physical quantity. Moreover, for better imaging quality, the approach should have the capacity to eliminate the low-resolution curse made by discretization. Therefore, we propose to represent the scatterer's relative permittivity distribution via Implicit Neural Representations (INR), as INR has remarkable capability in modeling location-dependent relationships [39, 51]. Its flexibility in handling image resolutions [10, 11, 29] also helps to *alleviate the curse made by discretization*. Besides, INR is known for its case-by-case optimization strategy, which can faithfully reflect each object's internal differences. In addition, INRs exhibit a strong capacity to recover information from incomplete data across a range of tasks [31, 32, 39], which can address the difficulties caused by sparse measurement. We then optimize the INR of each object by making sure that this representation can produce results akin to the actual measurements. Such an optimization based on forward estimation can help to *address the difficulties caused by inverse estimation*. Once the optimization settles down, we can access the relative permittivity values by using their corresponding locations and visualize them for imaging purposes.

Our solution is illustrated in Fig. 2. We use the Multilayer Perceptron (MLP) as the backbone of INR. Specifically, two MLPs are used to represent the relative permittivity and the induced current. It allows us to bypass complex matrix inversions in optimization, largely reducing the computational cost. To optimize the implicit representations, we propose to use a data loss and a state loss by fully considering the relationships between various physical quantities in the scattering process. Meanwhile, a random sampling strategy is designed for comprehensive consideration of each spatial position during optimization. Our primary contributions can be summarized as follows:

- We propose a solution to EISP based on forward estimation to avoid difficulties triggered by inverse estimation.
- We introduce the use of the learnable INR for the object's relative permittivity distribution to indicate the location-dependent quantity and achieve flexibility in imaging resolution.
- We explore a novel strategy that utilizes two separate MLPs for two physical quantities to avoid complex computations caused by matrix inversion.

The research for solving EISP has established standard benchmarks for evaluation [9, 53, 57]. We strictly follow these standard benchmarks in our research, including system settings, datasets, and metrics.

2   Related work

Electromagnetic inverse scattering problems (EISP). Conventional approaches for EISP can be classified as non-iterative and iterative categories.

Non-iterative methods tackle nonlinear issues by converting them into linear equations, such as the Born approximation [52], Rytov approximation [20, 27], and back-propagation (BP) method [2]. Since non-iterative methods are limited by reconstruction quality, other methods, such as the Subspace Optimization Method (SOM) [8, 60, 67], Contrast Source Inversion (CSI) Method [4, 28], Distorted Born Iterative Method (DBIM) [21], and other Newton-type methods [41, 49], are proposed to solve this problem in an iterative way. Despite their feasibility, their performance is highly sensitive to the initial guess, which undermines their robustness. Neural networks have recently been employed to construct nonlinear mappings linking the dispersed fields and the obscure constitutive attributes of scatterers [23, 35]. Most methods consider EISP in two stages [34, 57, 59, 64], where traditional approaches [2, 52] are first employed to obtain coarse images, and then the trained image-to-image neural networks are used for post-processing. However, due to the lack of consideration for scattering mechanisms, those methods encounter nearly all the difficulties faced by deep learning [33, 46], which easily causes their post-processing efforts to fail. We consider an implicit forward approach to overcome the aforementioned difficulties by optimizing a trainable implicit representation within a forward process.

Implicit neural representations (INR). Implicit neural representations usually employ an MLP to map from local coordinates to the associated values on that coordinates [26,51,63], such as intensity for images and videos, or occupancy value for 3D volumes. **The basics of INR are briefly explained below**. INR is a neural network $F_\theta : \mathbf{x} \mapsto F_\theta(\mathbf{x})$ that continuously maps the coordinates $\mathbf{x}$ to the corresponding quantity of interest. For the data expressed as a function $\Phi : \mathbf{x} \mapsto \Phi(\mathbf{x})$, the INR F_θ is a solution to $F_\theta(\mathbf{x}) - \Phi(\mathbf{x}) = 0$. Typically, the weight of INR, θ, can be obtained through optimization. INR has shown its advantages in parameterizing geometry and learning priors over shapes, as demonstrated by DeepSDF [47], Occupancy Networks [38], and IM-Net [12]. A considerable amount of subsequent research has proposed volumetric rendering of 3D implicit representations, including Neural Radiance Fields (NeRF) [39] and its acceleration [6, 42], quality enhancement [13, 56, 70], and copyright protection [37]. In the realm of 2D image representation, CPPNs [54] first proposed the use of neural networks to parameterize images implicitly. SIRENs [51] proposed generalization across implicit representations of images via hypernetworks. X-Fields [3] parameterizes the Jacobian of pixel position with respect to view, time, and illumination. In this work, we employ INR as the backbone to represent the scatterer's properties, which is able to characterize the complex spatial correlation in EISP and produce better imaging quality.

3   Physical model of EISP

As shown in Fig. 1, for an EISP system, the object to be imaged is defined as the unknown scatterer, and the enclosed space is represented by a square Region of Interest (ROI) denoted by D. Transmitters and receivers are positioned around

D to emit electromagnetic waves and measure the scattered electromagnetic fields, respectively.

Generally, the data measurement process can be split into two stages. At the first stage, the induced current is excited as the electromagnetic waves from the transmitters interact with the scatterer, aka wave-scatterer interaction. Subsequently, the induced current serves as a radiation source, generating the scattered fields. The total electric fields within D can be described by Lippmann-Schwinger equation [16], aka state equation, as follows:

$$E^{\mathrm{t}}(\mathbf{x}) = E^{\mathrm{i}}(\mathbf{x}) + k_0^2 \int_D g\left(\mathbf{x}, \mathbf{x}'\right) J\left(\mathbf{x}'\right) d\mathbf{x}', \ \mathbf{x} \in D, \tag{1}$$

where $\mathbf{x}$ and $\mathbf{x}'$ are the spatial coordinates. E^{i} is the incident electric fields directly from transmitters, while E^{t} is the total electric fields consisting of the original incident fields coming directly from transmitters and the scattered fields coming from scatterers. k_0 is the wavenumber computed from the signal frequency, and g is the free space Green's function. The relationship between the induced current J and total electric fields E^{t} can be expressed as follows:

$$J(\mathbf{x}) = \xi(\mathbf{x})E^t(\mathbf{x}). \tag{2}$$

In Eq. (2), ξ is the contrast defined as $\xi(\mathbf{x}) = \varepsilon_r(\mathbf{x}) - 1$, where $\varepsilon_r(\mathbf{x})$ denotes the relative permittivity of the unknown scatterer.

The second equation describes the scattered fields as a reradiation of the induced current [16], aka data equation, as follows:

$$E^{\mathrm{s}}(\mathbf{x}) = k_0^2 \int_D g\left(\mathbf{x}, \mathbf{x}'\right) J\left(\mathbf{x}'\right) d\mathbf{x}', \ \mathbf{x} \in S, \tag{3}$$

where E^s is the scattered fields that can be measured by receivers at surface S around the ROI D.

Since the digital signal analysis is only available on discrete variables[5] [40,55], Eq. (1) to Eq. (3) are inevitably transformed to their discrete counterparts. Specifically, the ROI D is discretized into $M \times M$ square subunits and the method of moments [48] is employed to obtain the discrete scattered fields. The relationship between discrete contrast $\boldsymbol{\xi}$ and discrete relative permittivity $\boldsymbol{\varepsilon}_r$ can be expressed as $\boldsymbol{\xi} = \boldsymbol{\varepsilon}_r - 1$. Then, Eq. (1) can be reformulated as follows:

$$\mathbf{E}^{\mathrm{t}} = \mathbf{E}^{\mathrm{i}} + \mathbf{G}_D \cdot \mathbf{J}, \tag{4}$$

where $\mathbf{E}^{\mathrm{t}}$, $\mathbf{E}^{\mathrm{i}}$, and $\mathbf{J}$ are the discrete E^t, E^i, and J, respectively. $\mathbf{G}_D$ is discrete free space Green's function in D. The discrete version of Eq. (2) can be represented as follows [53]:

$$\mathbf{J} = \mathrm{Diag}(\boldsymbol{\xi}) \cdot \mathbf{E}^{\mathrm{t}}, \tag{5}$$

---

[5] Discrete variables are denoted using **bold letters** in our paper
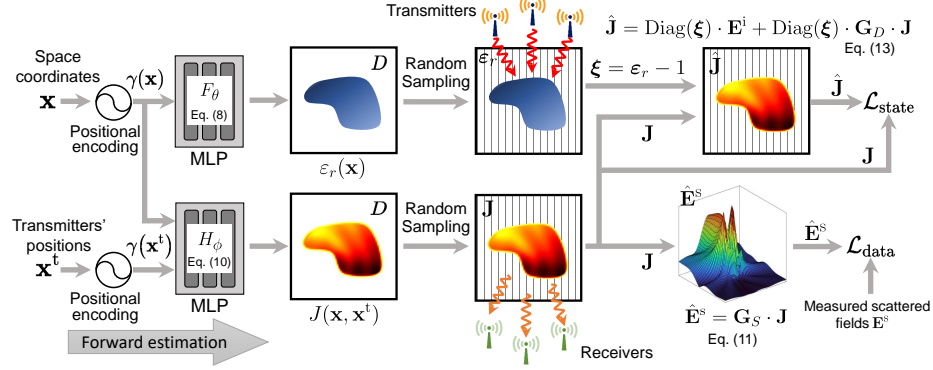
Fig. 2: Overview of our implicit method. Two MLPs, F_θ and H_ϕ, are used to implicitly represent relative permittivity ε_r and induced current J, respectively. Random sampling is applied for comprehensive optimization. The predicted induced current $\hat{\mathbf{J}}$ is calculated by Eq. (13) based on relative permittivity ε_r queried from F_θ and induced current J directly queried from H_ϕ. Then the state loss $\mathcal{L}_{\text{state}}$ is calculated by comparing the predicted $\hat{\mathbf{J}}$ and directly queried $\mathbf{J}$. Besides, the directly queried induced current $\mathbf{J}$ is used to compute the scattered fields $\hat{\mathbf{E}}^{\text{s}}$ by Eq. (11). Data loss function $\mathcal{L}_{\text{data}}$ is constructed to evaluate the difference between predicted scattered fields $\hat{\mathbf{E}}^{\text{s}}$ and the measured values $\mathbf{E}^{\text{s}}$.

where $\text{Diag}(\boldsymbol{\xi})$ is the diagonal matrix of contrast function. Similarly, Eq. (3) can be discretized as follows:

$$\mathbf{E}^{\text{s}} = \mathbf{G}_S \cdot \mathbf{J}, \tag{6}$$

where $\mathbf{E}^{\text{s}}$ is the discrete E^s, and $\mathbf{G}_S$ is the discrete Green's function to map contrast source $\mathbf{J}$ to scattered fields $\mathbf{E}^{\text{s}}$.

The task of EISP is to infer the relative permittivity ε_r, a value closely related to $\boldsymbol{\xi}$, *from the scattered fields* $\mathbf{E}^s$ *measured by receivers*, and then visualize it in an image. In an EISP system, knowing only $\mathbf{E}^{\text{i}}$ and $\mathbf{E}^{\text{s}}$ makes it challenging to estimate $\boldsymbol{\xi}$ inversely from $\mathbf{E}^{\text{s}}$ based on Eq. (6). Furthermore, the inherent nonlinearity originating from $\mathbf{G}_D \cdot \mathbf{J}$ in Eq. (4) complicates the estimation process [14, 18, 65]. Ultimately, ε_r, a variable with continuous characteristics, can only be derived using the aforementioned discrete equations, thereby compromising the imaging resolution. Consequently, an effective strategy is necessary to produce more accurate outcomes for EISP.

4   Proposed implicit solution

As depicted in Fig. 2, our fundamental idea is to solve the inverse scattering problem within a forward estimation process, which can be described by reformulating Eq. (4) to Eq. (6) as follows:

$$\mathbf{E}^{\text{s}} = \mathbf{G}_S \cdot \text{Diag}(\boldsymbol{\xi}) \cdot (\mathbf{I} - \mathbf{G}_D \text{Diag}(\boldsymbol{\xi}))^{-1} \cdot \mathbf{E}^{\text{i}}, \tag{7}$$

where $\mathbf{I}$ is the identity matrix. Contrary to previous approaches [2,52] that treat $\boldsymbol{\xi}$ as unknown, we regard the contrast $\boldsymbol{\xi}$ as a known quantity, by establishing relative permittivity ε_r involved in Eq. (2) as a learnable implicit representation. Then, we can calculate $\mathbf{E}^{\mathrm{s}}$ triggered by Eq. (7). During training, by contrasting the calculated $\mathbf{E}^{\mathrm{s}}$ with the measured true ones, the learnable representation can finally reach its optimum status. Since we do not aim to inversely express $\boldsymbol{\xi}$ as an explicit function of $\mathbf{E}^{\mathrm{s}}$, this optimization-in-forward approach can alleviate the challenges associated with inverse estimation and nonlinearity. The use of INR also ensures enhanced flexibility in imaging resolution. During inference, we can directly obtain the relative permittivity values by querying the representation with the corresponding coordinates.

4.1 Continuous representation for EISP

Representation for relative permittivity. We use a multilayer perceptron (MLP) with parameters θ to map the continuous spatial coordinates $\mathbf{x}$ to its associating relative permittivity values, which can be briefly described as follows:

$$\varepsilon_r(\mathbf{x}) = F_\theta\left(\gamma(\mathbf{x})\right), \tag{8}$$

where $\varepsilon_r{}^6$ denotes the relative permittivity obtained by querying the spatial coordinates within the continuous representation F_θ. We further apply the positional encoding for $\mathbf{x}$ to facilitate the fitting capability of the model as follows:

$$\gamma(\mathbf{x}) = \left[\sin\mathbf{x}, \cos\mathbf{x}, \cdots, \sin 2^{\Omega-1}\mathbf{x}, \cos 2^{\Omega-1}\mathbf{x}\right]^\top, \tag{9}$$

where Ω is a hyperparameter controlling the spectral bandwidth.

To optimize this continuous representation, we apply a series of equations defined by the computation of forward estimation, and then compare the scattered fields incited by this representation with the measured true ones. As discussed in Sec. 3, since the discretization is unavoidable during the forward computation, we only query discrete spatial coordinates during optimization to align with the discretization policy set by the method of moments [48]. Though we can directly perform the forward computation via Eq. (7), the computation complexity caused by its internal matrix inversion places a high demand on computing resources and potentially compromises the stability of problem-solving [25].

Representation for induced current. To avoid the complexity caused by matrix inversion, instead of the explicit computation defined in Eq. (7), we implicitly represent $\mathbf{J}$ as its continuous form using another MLP. By analyzing Eq. (7), the induced current is related to two variables: the discrete contrast $\boldsymbol{\xi}$ and the incident electric fields $\mathbf{E}^{\mathrm{i}}$ caused by transmitters. To faithfully describe such correlation, we propose to consider the representation for J as the mapping based on the spatial coordinates $\mathbf{x}$ and the transmitter's position $\mathbf{x}^{\mathrm{t}}$, which can be defined as follows:

$$J(\mathbf{x}, \mathbf{x}^{\mathrm{t}}) = H_\phi\left(\gamma(\mathbf{x}), \gamma(\mathbf{x}^{\mathrm{t}})\right), \tag{10}$$

---

[6] Due to its continuous property, we do not write it as bold font.

where H_ϕ is a continuous function consisting of fully connected networks.

Random spatial sampling. Due to the necessity of discretization in numerical computations to perform forward process, we need to spatially query the representations F_θ and H_ϕ at some positions to obtain their discrete forms. A typical approach is to divide the ROI D evenly into grids and deterministically sample the center location of each grid [36, 50]. However, the representations would only be queried at a fixed discrete set of locations in this way [39]. To take a comprehensive consideration of each spatial position, we use a random sampling scheme where we partition ROI D into $M \times M$ evenly-spaced grids, and the center of (m, n) grid is (x_m, y_n). Each sample location $(x_m^{\mathrm{sample}}, y_n^{\mathrm{sample}})$ is then randomly drawn from a Gaussian distribution: $x_m^{\mathrm{sample}} \sim \mathcal{N}(x_m, \sigma^2), \quad y_n^{\mathrm{sample}} \sim \mathcal{N}(y_n, \sigma^2)$, where σ is a hyperparameter to control the dispersion level of sample points around their means. By probabilistically sampling each spatial position, this scheme can alleviate the overlook of specific locations.

4.2   Forward calculation based optimization

The continuous representations obtained before can estimate corresponding physical quantities using spatial coordinates, but optimizing them directly with estimated values is hard because obtaining their true values is difficult [58]. Therefore, we indirectly refine the representations denoted by F_θ and H_ϕ by proposing a data loss and a state loss while fully considering the physical relationships.

Data loss. Based on Sec. 3, the wave-scatterer interaction leads to the induced current when the electromagnetic waves from transmitters interact with the scatterer. Then, the induced current generates the scattered fields, which can be measured by receivers. Thus, a straightforward way to refine the representations is to minimize the distance between the scattered fields computed from the representations and the true ones. With the discrete induced current $\mathbf{J}$ sampling from the continuous representation H_ϕ defined in Eq. (10), we can obtain the predicted scattered fields by reformulating the data equation in Eq. (6) as follows:

$$\hat{\mathbf{E}}_p^{\mathrm{s}} = \mathbf{G}_S \cdot \mathbf{J}_p, \tag{11}$$

where $\mathbf{G}_S$ denotes the discrete Green's function, and $\mathbf{J}_p$ and $\hat{\mathbf{E}}_p^{\mathrm{s}}$ denotes the discrete induced current and predicted scattered fields inspired by the p-th transmitter, respectively.

We then define our data loss used to contrast the predicted scattered fields with the measured true ones as follows:

$$\mathcal{L}_{\mathrm{data}} = \sum_{p=1}^{N_{\mathrm{t}}} \|\hat{\mathbf{E}}_p^{\mathrm{s}} - \mathbf{E}_p^{\mathrm{s}}\|^2, \tag{12}$$

where $\mathbf{E}_p^{\mathrm{s}}$ is the true scattered fields measured by receivers, and N_t denotes the number of all transmitters. The data loss enhances the optimization of the representation by accounting for discrepancies associated with all transmitters.

State loss. Although the data loss is straightforward, it cannot be used to optimize F_θ. Since the induced current $\mathbf{J}_p$ is directly obtained by querying its representation H_ϕ, Eq. (12) does not contain any variables related to F_θ. To effectively optimize F_θ, we consider minimizing the mismatch emerging from the state equation defined in Eq. (4) and Eq. (5). Specifically, by reformulating Eq. (7), an expression related to p-th transmitter can obtained as follows:

$$\hat{\mathbf{J}}_p = \mathrm{Diag}(\boldsymbol{\xi}) \cdot \mathbf{E}_p^{\mathrm{i}} + \mathrm{Diag}(\boldsymbol{\xi}) \cdot \mathbf{G}_D \cdot \mathbf{J}_p, \tag{13}$$

where $\mathbf{J}_p$ denotes the discrete induced current sampling from H_ϕ, $\boldsymbol{\xi}$ denotes the contrast, and $\hat{\mathbf{J}}_p$ indicates the induced current computed via the above mathematical correlation.

Although $\mathbf{J}_p$ and $\hat{\mathbf{J}}_p$ originate from distinct sources, both represent the induced current values within the same spatial domain. If the same spatial coordinates are given, they should yield identical values irrespective of their generation sources. Therefore, we introduce a state loss to minimize the mismatch between $\mathbf{J}_p$ and $\hat{\mathbf{J}}_p$ as follows:

$$\mathcal{L}_{\mathrm{state}} = \sum_{p=1}^{N_{\mathrm{t}}} \|\hat{\mathbf{J}}_p - \mathbf{J}_p\|^2, \tag{14}$$

where N_{t} is the number of all transmitters. Since Eq. (2) has clearly defined the close correlation between $\boldsymbol{\xi}$ and the permittivity values ε_r, the minimization of the state loss can ultimately optimize F_θ and H_ϕ used for representing the relative permittivity and induced current, respectively.

Overall loss. The overall loss to train the relative permittivity representation F_θ and induced current representation H_ϕ can be obtained as $\mathcal{L} = \lambda_{\mathrm{data}}\mathcal{L}_{\mathrm{data}} + \lambda_{\mathrm{state}}\mathcal{L}_{\mathrm{state}} + \lambda_{\mathrm{TV}}\mathcal{L}_{\mathrm{TV}}$, where $\mathcal{L}_{\mathrm{TV}}$ is a total variation loss for $\boldsymbol{\xi}$, and λ_{data}, λ_{state}, λ_{TV} are hyperparameters to balance the loss functions.

4.3 Implementation details

We implement our method using PyTorch. Two eight-layer MLPs with 256 channels and ReLU activations are used to predict the relative permittivity ε_r and induced current J, respectively. Similar to the settings in previous methods based on INRs [39, 51], positional encoding is applied to input positions before they are passed into the MLPs. The ROI D is discretized into 64×64 while training. The hyperparameters for the overall loss are set as $\lambda_{\mathrm{data}} = 1.00$, $\lambda_{\mathrm{state}} = 1.00$, and $\lambda_{\mathrm{TV}} = 0.01$. We use the Adam optimizer with default values $\beta_1 = 0.9$, $\beta_2 = 0.999$, $\epsilon = 10^{-8}$, and a learning rate 5×10^{-4} that decays following the exponential scheduler during the optimization. We optimize the model for 4K iterations on a single NVIDIA V100 GPU for all the datasets.

5 Experiments

5.1 Experiment setup

Dataset. We strictly follow the established rules in EISP [36, 53, 57] to set the dataset. We train and test our model on **standard benchmarks** used for EISP.
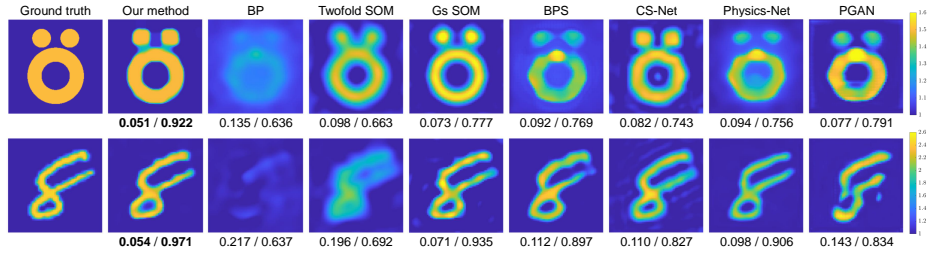
1) Synthetic **Circular-cylinder dataset** is synthetically generated comprising 1200 images of cylinders with random relative radius, number, and location and permittivity between 1 and 1.5. 2) Synthetic **MNIST dataset** contains grayscale images of handwritten digits. Similar to previous settings [57, 69], we randomly select 1200 of them to synthesize scatterers with relative permittivity values between 2 and 2.5 according to their corresponding pixel values. Following previous work to generate the above two synthetic datasets, we use 16 transmitters and 32 receivers equally placed on a circle for regular settings, and the data are generated numerically using the method of moments [48] with a 224×224 grid mesh to avoid inverse crime [17]. For sparse measurement experiments, we decrease the number of receivers from 32 to 8 to utilize only 25% of the regular measurement data. 3) Real-world **Institut Fresnel's database** contains three different dielectric scenarios, namely FoamDielExt, FoamDielInt, and FoamTwinDiel. There are 8 transmitters for FoamDielExt and FoamDielInt, 18 transmitters for FoamTwinDiel, and 241 receivers for all the cases. As the wavelength of the emitted electromagnetic wave should be comparable to or smaller than the size of the target object, we set operating frequency $f = 400$ MHz on synthetic datasets, and $f = 5$ GHz on real-world datasets.

Baselines. We maintain the same settings as in previous studies [50,53,57] to ensure a fair comparison. We compare our method with three traditional methods and four deep learning-based approaches: 1) **BP** [2]: A traditional non-iterative inversion algorithm. 2) **Twofold SOM** [66]: A traditional iterative minimization scheme by using SVD decomposition. 3) **Gs SOM** [8]: A traditional subspace-based optimization method by decomposing the operator of Green's function. 4) **BPS** [57]: A CNN-based image translation method with an initial guess from the BP algorithm. 5) **CS-Net** [50]: A CNN-based contrast source reconstruction scheme via subspace optimization. 6) **Physics-Net** [36]: A CNN-based approach that incorporates physical phenomena during training. 7) **PGAN** [53]: A CNN-based approach using a generative adversarial network.

Evaluation methodology. We evaluate the quantitative performance of our method using PSNR, SSIM, and Relative Root-Mean-Square Error (RRMSE) [53]. For PSNR and SSIM, a higher value indicates better performance. For RRMSE [53], a lower value indicates better performance. RRMSE is a metric widely used in EISP defined as RRMSE $= (\frac{1}{M \times M} \sum_{m=1}^{M} \sum_{n=1}^{M} |\frac{\hat{\varepsilon}_r(m,n) - \varepsilon_r(m,n)}{\varepsilon_r(m,n)}|^2)^{\frac{1}{2}}$, where $\varepsilon_r(m,n)$ and $\hat{\varepsilon}_r(m,n)$ are the true and reconstructed discrete relative permittivity of the unknown scatterers at location (m,n), respectively, and $M \times M$ is the total number of subunits over the ROI D.

5.2   Experiment results

Qualitative results on synthetic data. We first compare the reconstruction quality visually using synthetic data including circular-cylinder dataset [57] and MNIST dataset [19] against all baselines and the results are shown in Fig. 3. Our method achieves superior visual performance compared to all other baselines. Traditional methods, such as BP [2] and Twofold SOM [66], can only recover the

Fig. 3: Samples obtained from synthetic Circular-cylinder dataset and MNIST dataset. From left to right: ground truth, results obtained using our method, BP [2], Twofold SOM [66], Gs SOM [8], BPS [57], CS-Net [50], Physics-Net [36], and PGAN [53]. The pixel values in the images indicate the values of the relative permittivity. RRMSE/SSIM values are shown below each figure. The first row is a standard test case [1, 57], a well-known pattern for the evaluation of EISP methods.
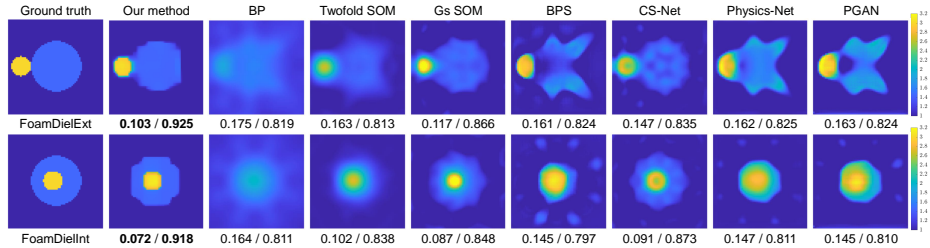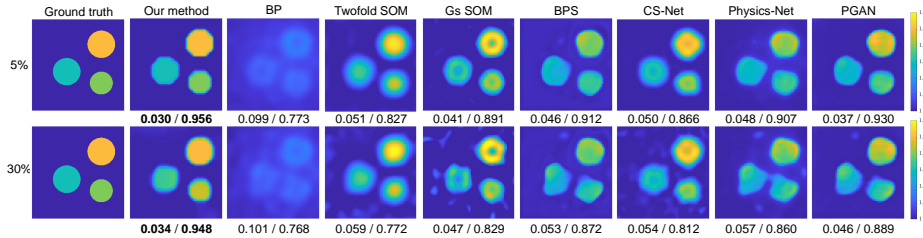

Fig. 4: Samples obtained from real-world Institut Fresnel's database. From left to right: ground truth, results obtained using our method, BP [2], Twofold SOM [66], Gs SOM [8], BPS [57], CS-Net [50], Physics-Net [36], and PGAN [53]. The pixel values in the images indicate the values of the relative permittivity. RRMSE/SSIM values are shown below each figure.

rough shape of the target and produce inaccurate results at some junction parts. Gs SOM [8] can reconstruct the relative permittivity of the targets with relatively high accuracy, but still has obvious visual defects. Though deep learning-based methods, such as BPS [57], CS-Net [50], Physics-Net [36], and PGAN [53], can produce more accurate estimation, their visual qualities are still far below our proposed method.

Qualitative results on real-world data. We further test our algorithm on real-world data. The results for all methods are shown in Fig. 4. The visual performance of our method remains superior when applied to real-world data. Conventional methods exhibit a diminished performance, which, when used as input, further negatively impacts the efficacy of deep learning-based approaches.

Noise robustness. We also compare the robustness of the models. By adding different levels of noise to the received scattered fields signal, we use the noisy scattered fields signal to recover the scattered object. The results are shown in Fig. 5. It can be observed that when large noise is added, the results of other

Fig. 5: Samples obtained under 5% and 30% noise levels. From left to right: ground truth, results obtained using our method, BP [2], Twofold SOM [66], Gs SOM [8], BPS [57], CS-Net [50], Physics-Net [36], and PGAN [53]. The pixel values in the images indicate the values of the relative permittivity. RRMSE/SSIM values are shown below each figure.

Table 1: Quantitative evaluation compared with BP [2], Twofold SOM [66], Gs SOM [8], BPS [57], CS-Net [50], Physics-Net [36], and PGAN [53]. Best results are shown in **bold**.

	Circular dataset (5%)			Circular dataset (30%)			MNIST dataset (5%)			MNIST dataset (30%)			Institut Fresnel's database		
	RRMSE	SSIM	PSNR	RRMSE	SSIM	PSNR	RRMSE	SSIM	PSNR	RRMSE	SSIM	PSNR	RRMSE	SSIM	PSNR
Proposed	**0.016**	**0.968**	**39.20**	**0.027**	**0.938**	**34.15**	**0.017**	**0.972**	**37.90**	**0.044**	**0.893**	**29.70**	**0.127**	**0.897**	**27.06**
BP	0.048	0.916	28.96	0.049	0.914	28.94	0.171	0.750	20.02	0.174	0.744	19.87	0.180	0.792	17.74
Twofold SOM	0.035	0.917	32.27	0.040	0.880	31.13	0.137	0.770	22.35	0.142	0.745	22.13	0.149	0.804	23.87
Gs SOM	0.034	0.926	32.74	0.035	0.916	32.43	0.101	0.853	24.63	0.113	0.811	23.73	0.135	0.837	24.95
BPS	0.027	0.964	34.20	0.034	0.928	32.17	0.098	0.912	25.68	0.133	0.859	23.21	0.166	0.787	18.86
CS-Net	0.024	0.900	33.75	0.035	0.810	31.27	0.179	0.788	25.37	0.227	0.724	24.15	0.137	0.828	24.87
Physics-Net	0.024	0.945	37.20	0.031	0.921	33.53	0.079	0.938	27.74	0.113	0.889	24.44	0.168	0.795	18.42
PGAN	0.021	0.957	36.89	0.030	0.933	33.03	0.090	0.918	26.09	0.124	0.873	23.64	0.167	0.794	18.46

baselines are greatly affected. However, our method can accurately reconstruct the scatterer under larger noise, demonstrating the superior robustness of the proposed method.

Evaluation for flexible resolution. The continuity of implicit function allows INR to interpolate and infer at arbitrary points in the input space. This characteristic ensures flexible resolution during the imaging process. As depicted in Fig. 6, we employ a fixed resolution of 64×64 during training and acquire images of varying resolutions by sampling the INR at different scales. The use of the random sampling scheme can avoid artifacts in the results. Compared to post-super-resolution methods, like Gs SOM + HAT-L [7], our method can achieve higher quality results. The resolution flexibility of INR paves the way for more in-depth analysis of reconstructed images at various resolution levels.

Quantitative results. The quantitative results of the reconstruction quality in Tab. 1 further validate the proposed method. Higher PSNR and SSIM values suggest our method accurately recovers object shapes and effectively maintains detailed structural information. Lower relative error values indicate our method's predictions of relative permittivity distribution are more accurate compared to other methods.

Results for sparse measurement. We use 25% of the standard measurement data to conduct an experiment [50, 57], and the results are shown in Fig. 7.
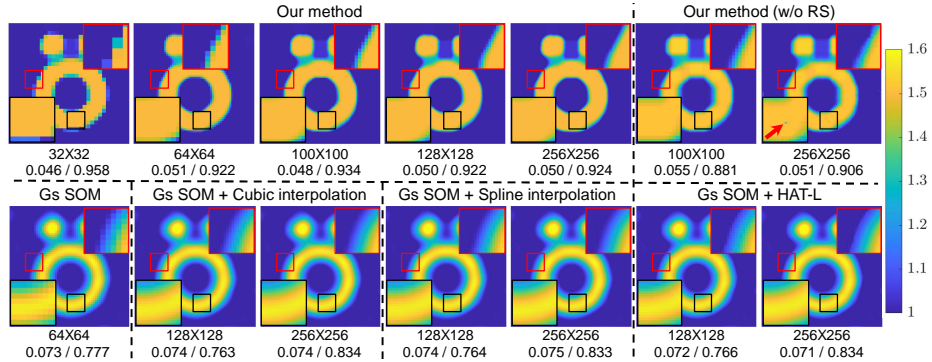
Fig. 6: Comparison of resolution flexibility among different methods. Our method is evaluated against our method without random sampling (RS) scheme, Gs SOM [8], Gs SOM + Cubic/Spline interpolation, and Gs SOM + HAT-L [7], under different resolution settings. All methods are implemented at an original resolution of 64×64. The pixel values in the images indicate the values of the relative permittivity. Resolution and RRMSE/SSIM values are shown below each figure.
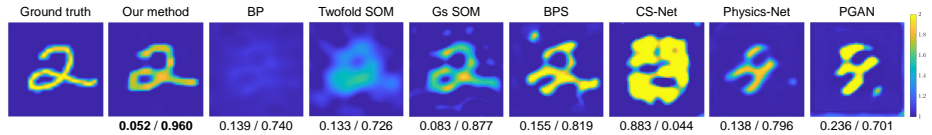

Fig. 7: The results for sparse measurement. From left to right: ground truth, results obtained using our method, BP [2], Twofold SOM [66], Gs SOM [8], BPS [57], CS-Net [50], Physics-Net [36], and PGAN [53]. The pixel values in the images indicate the values of the relative permittivity. RRMSE/SSIM values are shown below each figure.

Our method, leveraging INR, shows superior capability in reconstructing the object's interior from sparse measurements compared with other methods. This also demonstrates that INR is more suitable for representing the relative permittivity distribution of the object compared to other matrix-based representations like Twofold SOM [66] and CS-Net [50].

Results for 3D scenarios. Our method can naturally generalize to 3D scenarios. In 3D scenarios, we utilize 3D Green's functions in Eq. (4) and Eq. (6), and perform integration over a 3D region of interest. We augment the input dimension of representations for relative permittivity and induced current to align with the 3D coordinates, while keeping the remaining structures unchanged. We collect the 3D scattering data from the synthetic 3D MNIST dataset [30] and real-world dataset [22]. In the synthetic experiments, we employ 40 transmitters and 160 receivers arranged around a unit cube. The results shown in Fig. 8 demonstrate that our method can reconstruct 3D objects by solving EISP.

Time analysis. Our method, BP [2], Twofold SOM [66], and Gs SOM [8] are case-specific methods that do not require additional training time. The BPS [57], CS-Net [50], Physics-Net [36], and PGAN [53] are deep-learning methods that
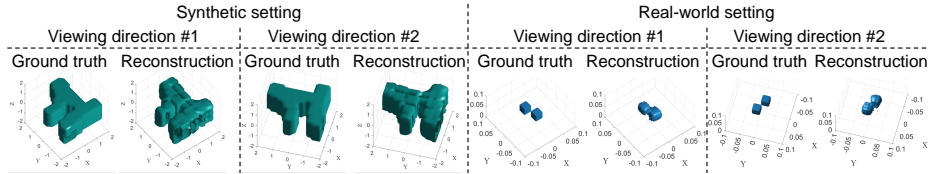
Fig. 8: The results for 3D scenarios on 3D MINIST dataset [30] and real-world dataset [22]. We show two example cases with three viewing directions. We use isosurface to visualize the ground truths and reconstructed results of the spatial distribution of relative permittivity.

Table 2: Ablation results compared with single representation for relative permittivity.

	Parameter counts↓	Time each iteration↓	RRMSE↓	SSIM↑	PSNR↑
Proposed	1,019,139	**117 ms**	**0.038**	**0.909**	**30.36**
Single representation	**493,313**	289 ms	0.053	0.876	27.32

necessitate model training. We count the time for optimization procedure in inference time, and our method outperforms traditional case-specific methods and CS-Net [50]. Although the inference of other deep-learning methods is very fast, their training processes are time-consuming. Additionally, we may be able to reduce the optimization time through modifying the INR structure [42] or improving the training process [61, 62].

Ablation study Our approach mainly consists of three parts: the representation for relative permittivity, representation for induced current, and random sampling. Since both the data loss $\mathcal{L}_{\mathrm{data}}$ and the state loss $\mathcal{L}_{\mathrm{state}}$ are necessary for our method, we cannot easily remove any of them. We first use a single representation for relative permittivity to replace the two MLPs in our original approach. Both models are trained on an NVIDIA V100 GPU. From the results shown in Tab. 2, the model with a single MLP takes a longer iteration time to achieve similar performance. We further remove the random sampling scheme and adopt a uniform sampling approach. As shown in the last two columns in Fig. 6, results without random sampling have lower metric values, and the high-resolution results occasionally meet obvious artifacts.

6   Conclusions

An implicit solution is presented to the EISP in this paper. We propose implicitly representing the unknown scatterer's relative permittivity distribution as a trainable representation and optimizing these representations within a forward estimation process. A two-MLP strategy is employed to reduce the computation complexity. The experimental results on synthetic and real-world data demonstrate the promising performance of our proposed method. We will further collaborate with other parties to consider our solution in different scenarios, such as medical diagnostics, in more challenging conditions.

Acknowledgments

References

1. Belkebir, K., Tijhuis, A.: Using multiple frequency information in the iterative solution of a two-dimensional nonlinear inverse problem. In: Proceedings Progress in Electromagnetics Research Symposium (1996)
2. Belkebir, K., Chaumet, P.C., Sentenac, A.: Superresolution in total internal reflection tomography. Journal of the Optical Society of America A (2005)
3. Bemana, M., Myszkowski, K., Seidel, H.P., Ritschel, T.: X-fields: Implicit neural view-, light-and time-image interpolation. ACM Transactions on Graphics (TOG) (2020)
4. van den Berg, P.M., Van Broekhoven, A., Abubakar, A.: Extended contrast source inversion. Inverse problems (1999)
5. Bevacqua, M.T., Di Meo, S., Crocco, L., Isernia, T., Pasian, M.: Millimeter-waves breast cancer imaging via inverse scattering techniques. IEEE Journal of Electromagnetics, RF and Microwaves in Medicine and Biology (2021)
6. Chen, A., Xu, Z., Geiger, A., Yu, J., Su, H.: TensoRF: Tensorial radiance fields. In: Proceedings of the European Conference on Computer Vision (2022)
7. Chen, X., Wang, X., Zhou, J., Qiao, Y., Dong, C.: Activating more pixels in image super-resolution transformer. In: Proceedings of the IEEE/CVF Conference on Computer Vision and Pattern Recognition (2023)
8. Chen, X.: Subspace-based optimization method for solving inverse-scattering problems. IEEE Transactions on Geoscience and Remote Sensing (2009)
9. Chen, X.: Computational methods for electromagnetic inverse scattering. John Wiley & Sons (2018)
10. Chen, Y., Liu, S., Wang, X.: Learning continuous image representation with local implicit image function. In: Proceedings of the IEEE/CVF Conference on Computer Vision and Pattern Recognition (2021)
11. Chen, Z., Chen, Y., Liu, J., Xu, X., Goel, V., Wang, Z., Shi, H., Wang, X.: Videoinr: Learning video implicit neural representation for continuous space-time super-resolution. In: Proceedings of the IEEE/CVF Conference on Computer Vision and Pattern Recognition (2022)
12. Chen, Z., Zhang, H.: Learning implicit fields for generative shape modeling. In: Proceedings of the IEEE/CVF Conference on Computer Vision and Pattern Recognition (2019)
13. Cheng, Y., Wan, R., Weng, S., Zhu, C., Chang, Y., Shi, B.: Colorizing monochromatic radiance fields. In: Proceedings of the AAAI Conference on Artificial Intelligence (2024)

14. Chew, W.C.: Waves and fields in inhomogenous media, vol. 16. John Wiley & Sons (1999)
15. Chew, W.C., Wang, Y.M.: Reconstruction of two-dimensional permittivity distribution using the distorted Born iterative method. IEEE Transactions on Medical Imaging (1990)
16. Colton, D., Kress, R.: Integral Equation Methods in Scattering Theory. SIAM (2013)
17. Colton, D.L., Kress, R., Kress, R.: Inverse Acoustic and Electromagnetic Scattering Theory. Springer (1998)
18. Cui, T.J., Chew, W.C., Yin, X.X., Hong, W.: Study of resolution and super resolution in electromagnetic imaging for half-space problems. IEEE Transactions on Antennas and Propagation (2004)
19. Deng, L.: The MNIST database of handwritten digit images for machine learning research. IEEE Signal Processing Magazine (2012)
20. Devaney, A.: Inverse-scattering theory within the rytov approximation. Optics Letters (1981)
21. Gao, F., Van Veen, B.D., Hagness, S.C.: Sensitivity of the distorted born iterative method to the initial guess in microwave breast imaging. IEEE Transactions on Antennas and Propagation (2015)
22. Geffrin, J., Sabouroux, P.: Continuing with the fresnel database: experimental setup and improvements in 3d scattering measurements. Inverse Problems (2009)
23. Geng, R., Hu, Y., Chen, Y., et al.: Recent advances on non-line-of-sight imaging: Conventional physical models, deep learning, and new scenes. APSIPA Transactions on Signal and Information Processing (2021)
24. Geng, R., Li, Y., Zhang, D., Wu, J., Gao, Y., Hu, Y., Chen, Y.: Dream-pcd: Deep reconstruction and enhancement of mmwave radar pointcloud. arXiv preprint arXiv:2309.15374 (2023)
25. Golub, G.H., Van Loan, C.F.: Matrix Computations. JHU Press (2013)
26. Grattarola, D., Vandergheynst, P.: Generalised implicit neural representations. In: Advances in Neural Information Processing Systems (2022)
27. Habashy, T.M., Groom, R.W., Spies, B.R.: Beyond the born and rytov approximations: A nonlinear approach to electromagnetic scattering. Journal of Geophysical Research: Solid Earth (1993)
28. Habashy, T.M., Oristaglio, M.L., de Hoop, A.T.: Simultaneous nonlinear reconstruction of two-dimensional permittivity and conductivity. Radio Science (1994)
29. Hu, H., Chen, Y., Xu, J., Borse, S., Cai, H., Porikli, F., Wang, X.: Learning implicit feature alignment function for semantic segmentation. In: European Conference on Computer Vision (2022)
30. de la Iglesia Castro, D.: 3D mnist: A 3D version of the mnist database of handwritten digits. https://www.kaggle.com/datasets/daavoo/3d-mnist
31. Jagatap, G., Hegde, C.: Phase retrieval using untrained neural network priors. In: NeurIPS 2019 Workshop on Solving Inverse Problems with Deep Networks (2019)
32. Lempitsky, V., Vedaldi, A., Ulyanov, D.: Deep image prior. In: IEEE/CVF Conference on Computer Vision and Pattern Recognition (2018)
33. Li, J., Pang, M., Dong, Y., Jia, J., Wang, B.: Graph neural network explanations are fragile. In: International Conference on Machine Learning (2024)
34. Li, L., Wang, L.G., Teixeira, F.L., Liu, C., Nehorai, A., Cui, T.J.: Deepnis: Deep neural network for nonlinear electromagnetic inverse scattering. IEEE Transactions on Antennas and Propagation (2018)

35. Li, Y., Zhang, D., Geng, R., Wu, J., Hu, Y., Sun, Q., Chen, Y.: Ifnet: Imaging and focusing network for handheld mmwave devices. In: IEEE International Conference on Acoustics, Speech and Signal Processing (ICASSP) (2024)

36. Liu, Z., Roy, M., Prasad, D.K., Agarwal, K.: Physics-guided loss functions improve deep learning performance in inverse scattering. IEEE Transactions on Computational Imaging (2022)

37. Luo, Z., Guo, Q., Cheung, K.C., See, S., Wan, R.: Copyrnerf: Protecting the copyright of neural radiance fields. In: Proceedings of the IEEE/CVF International Conference on Computer Vision (2023)

38. Mescheder, L., Oechsle, M., Niemeyer, M., Nowozin, S., Geiger, A.: Occupancy networks: Learning 3D reconstruction in function space. In: Proceedings of the IEEE/CVF Conference on Computer Vision and Pattern Recognition (2019)

39. Mildenhall, B., Srinivasan, P.P., Tancik, M., Barron, J.T., Ramamoorthi, R., Ng, R.: NeRF: Representing scenes as neural radiance fields for view synthesis. In: Proceedings of the European Conference on Computer Vision (2020)

40. Mitra, S.K.: Digital signal processing: a computer-based approach. McGraw-Hill Higher Education (2001)

41. Mojabi, P., LoVetri, J.: Comparison of te and tm inversions in the framework of the gauss-newton method. IEEE Transactions on Antennas and Propagation (2010)

42. Müller, T., Evans, A., Schied, C., Keller, A.: Instant neural graphics primitives with a multiresolution hash encoding. ACM Transactions on Graphics (ToG) (2022)

43. Nikolova, N.K.: Microwave imaging for breast cancer. IEEE Microwave Magazine (2011)

44. Nordebo, S., Gustafsson, M., Nilsson, B.: Fisher information analysis for two-dimensional microwave tomography. Inverse Problems (2007)

45. O'Loughlin, D., O'Halloran, M., Moloney, B.M., Glavin, M., Jones, E., Elahi, M.A.: Microwave breast imaging: Clinical advances and remaining challenges. IEEE Transactions on Biomedical Engineering (2018)

46. Pang, M., Wang, B., Ye, M., Cheung, Y.M., Zhou, Y., Huang, W., Wen, B.: Heterogeneous prototype learning from contaminated faces across domains via disentangling latent factors. IEEE Transactions on Neural Networks and Learning Systems (2024)

47. Park, J.J., Florence, P., Straub, J., Newcombe, R., Lovegrove, S.: Deepsdf: Learning continuous signed distance functions for shape representation. In: Proceedings of the IEEE/CVF Conference on Computer Vision and Pattern Recognition (2019)

48. Peterson, A.F., Ray, S.L., Mittra, R.: Computational methods for electromagnetics. IEEE Press New York (1998)

49. Rubæk, T., Meaney, P.M., Meincke, P., Paulsen, K.D.: Nonlinear microwave imaging for breast-cancer screening using gauss–newton's method and the cgls inversion algorithm. IEEE Transactions on Antennas and Propagation (2007)

50. Sanghvi, Y., Kalepu, Y., Khankhoje, U.K.: Embedding deep learning in inverse scattering problems. IEEE Transactions on Computational Imaging (2019)

51. Sitzmann, V., Martel, J., Bergman, A., Lindell, D., Wetzstein, G.: Implicit neural representations with periodic activation functions. In: Advances in Neural Information Processing Systems (2020)

52. Slaney, M., Kak, A., Larsen, L.: Limitations of imaging with first-order diffraction tomography. IEEE Transactions on Microwave Theory and Techniques (1984)

53. Song, R., Huang, Y., Xu, K., Ye, X., Li, C., Chen, X.: Electromagnetic inverse scattering with perceptual generative adversarial networks. IEEE Transactions on Computational Imaging (2021)

54. Stanley, K.O.: Compositional pattern producing networks: A novel abstraction of development. Genetic programming and evolvable machines (2007)
55. Taflove, A., Hagness, S.C., Piket-May, M.: Computational electromagnetics: the finite-difference time-domain method. The Electrical Engineering Handbook (2005)
56. Tang, Y., Zhu, C., Wan, R., Xu, C., Shi, B.: Neural underwater scene representation. In: Proceedings of the IEEE/CVF Conference on Computer Vision and Pattern Recognition (2024)
57. Wei, Z., Chen, X.: Deep-learning schemes for full-wave nonlinear inverse scattering problems. IEEE Transactions on Geoscience and Remote Sensing (2018)
58. Wei, Z., Chen, X.: Uncertainty quantification in inverse scattering problems with bayesian convolutional neural networks. IEEE Transactions on Antennas and Propagation (2020)
59. Xu, K., Zhang, C., Ye, X., Song, R.: Fast full-wave electromagnetic inverse scattering based on scalable cascaded convolutional neural networks. IEEE Transactions on Geoscience and Remote Sensing (2021)
60. Xu, K., Zhong, Y., Wang, G.: A hybrid regularization technique for solving highly nonlinear inverse scattering problems. IEEE Transactions on Microwave Theory and Techniques (2017)
61. Zhang, C., Cao, X., Liu, W., Tsang, I., Kwok, J.: Nonparametric iterative machine teaching. In: International Conference on Machine Learning (2023)
62. Zhang, C., Cao, X., Liu, W., Tsang, I., Kwok, J.: Nonparametric teaching for multiple learners. Advances in Neural Information Processing Systems (2023)
63. Zhang, C., Luo, S., Li, J., Wu, Y.C., Wong, N.: Nonparametric teaching of implicit neural representations. In: International Conference on Machine Learning (2024)
64. Zhang, L., Xu, K., Song, R., Ye, X., Wang, G., Chen, X.: Learning-based quantitative microwave imaging with a hybrid input scheme. IEEE Sensors Journal (2020)
65. Zhang, X., Zhao, Z.: A new scheme for solving highly nonlinear inverse scattering problems with noise disturbance. IEEE Geoscience and Remote Sensing Letters (2022)
66. Zhong, Y., Chen, X.: Twofold subspace-based optimization method for solving inverse scattering problems. Inverse Problems (2009)
67. Zhong, Y., Chen, X.: An fft twofold subspace-based optimization method for solving electromagnetic inverse scattering problems. IEEE Transactions on Antennas and Propagation (2011)
68. Zhong, Y., Lambert, M., Lesselier, D., Chen, X.: A new integral equation method to solve highly nonlinear inverse scattering problems. IEEE Transactions on Antennas and Propagation (2016)
69. Zhou, H., Cheng, Y., Zheng, H., Liu, Q., Wang, Y.: Deep unfolding contrast source inversion for strong scatterers via generative adversarial mechanism. IEEE Transactions on Microwave Theory and Techniques (2022)
70. Zhu, C., Wan, R., Tang, Y., Shi, B.: Occlusion-free scene recovery via neural radiance fields. In: Proceedings of the IEEE/CVF Conference on Computer Vision and Pattern Recognition (2023)